Supplementary Materials: Polymers and Plastrons in Parallel Yield Enhanced Turbulent Drag Reduction

Anoop Rajappan [1] and Gareth H. McKinley [1]*

1. Frictional drag measurements in turbulent Taylor-Couette flow

Frictional drag measurements in our study were performed using a bespoke Taylor-Couette (TC) flow apparatus with an improved design, based on the wide-gap TC geometry previously described by Srinivasan et al. [1] The rotating inner cylinder (rotor) is machined from aluminum 6061-T6 alloy, and has radius $R_i = 38.1\,\text{mm}$ and axial length $L = 76.2\,\text{mm}$; its exterior cylindrical surface was either polished smooth for no-slip flow measurements, or suitably processed to generate the grooved superhydrophobic texture for use in drag reduction tests (as described in §2 of this Supplemental Material). The stationary outer cylinder (stator) enclosing the rotor is made of transparent acrylic and has radius $R_o = 50.8\,\text{mm}$, creating an annular flow gap of width $d = R_o - R_i = 12.7\,\text{mm}$ in which the working fluid (water or dilute polymer solution) is contained; this yields a radius ratio of $\zeta = R_i/R_o = 0.75$ and a geometric aspect ratio of $L/d = 6.0$ for our particular TC geometry. The rotor is coupled to a commercial rotational rheometer (AR-G2, TA Instruments), which enables precise control of the rotor angular speed Ω, and accurate measurement of the steady-state frictional torque $\mathcal{T}$ exerted by the working fluid on the cylindrical rotor wall. The rotor incorporates a hollow interior recess designed to remain air-filled during experiments; this provides a shear-free boundary at the base that helps eliminate extraneous torque arising from fluid friction acting on the bottom face. The TC apparatus was extensively tested and characterized in the course of our prior experimental studies on drag-reducing superhydrophobic textures [2] and biopolymer solutions [3], and further details of its design and operational features may be found in these earlier reports.

As per the usual convention for TC flows, we define the Reynolds number $\text{Re} = \rho V d/\eta$ based on the gap width d, the azimuthal speed $V = R_i\Omega$ of the rotor wall, and the density ρ and viscosity η of the working fluid. As the angular speed Ω of the rotor is increased, the flow inside the cell gap progresses through a series of secondary vortical flow regimes, and eventually transitions to featureless, shear-driven turbulence when sufficiently large rotor speed (or Reynolds number) is reached. To determine the critical Reynolds number Re_{crit} at which the transition to this terminal turbulent flow regime occurs in our bespoke TC geometry, we adopted the method proposed by Lathrop et al. [4], and computed the torque exponent α from the baseline friction curve for a smooth, no-slip rotor:

$$\alpha = \frac{\mathrm{d}\log G}{\mathrm{d}\log \text{Re}}\,. \tag{1}$$

Here $G = \mathcal{T}/\rho\nu^2 L$ is the dimensionless frictional torque, and $\nu = \eta/\rho$ is the kinematic viscosity of the working fluid. The empirical value of α derived thus is shown in Fig. S1 as a function of the Reynolds number. As evident from the plot, a marked discontinuity in the slope of the curve is observed at $\text{Re} \simeq 11\,000$, indicating a change in the dependence of α on Re (and by extension, a change in the scaling of G with Re). Following Lathrop et al. [4], we identify $\text{Re}_{\text{crit}} = 11\,000$ as the critical Reynolds number at which the annular shear flow within the TC apparatus transitions to featureless wall-driven turbulence. Additional flow visualization experiments confirming this transition to featureless turbulent flow inside the cell gap can be found in Ref. [3].

In our study, flow measurements employing polymers or superhydrophobic surfaces were performed at $\text{Re} \geqslant 15\,000$, well into the turbulent flow regime; the extra allowance was intended as a precaution against possible effects of delayed transition or wall slip caused by the drag-reducing polymer or superhydrophobic surface under evaluation. A typical flow experiment consisted of varying the angular speed Ω of the rotor in discrete steps, and recording the mean steady-state frictional torque $\mathcal{T}$. The average shear stress $\tau_w = \mathcal{T}/2\pi R_i^2 L$ at the rotor wall, and the friction velocity

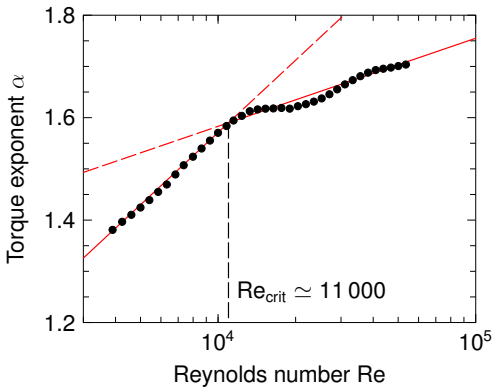

Figure S1. The experimental torque exponent α as a function of the Reynolds number Re.

$u_\tau = \sqrt{\tau_w/\rho}$ in the near-wall layer, were then obtained from the experimental data. Finally, the shear Reynolds number was computed based on the gap width as $\mathrm{Re}_\tau = \rho u_\tau d/\eta$, with the reference viscosity η set equal to either the viscosity of water η_w, or—in tests involving drag-reducing polymers—the zero shear viscosity η_0 of the dilute solution employed as the working fluid; the latter was determined independently during each experiment using an Ubbelöhde type glass capillary viscometer. Flow measurements were conducted at room temperature, (23.0 ± 0.5) °C, and multiple replicates were obtained for each flow curve and averaged. For tests employing the grooved superhydrophobic rotor, the working fluid was allowed to aerate inside a ventilated, partially-filled container for several hours before the experiment to attain air saturation at ambient temperature, with the aim of preventing undue depletion of the plastron layer by diffusion of gas into the liquid phase. Furthermore, in experiments involving polymer solutions, the test protocol was carefully designed to mitigate effects of flow-induced degradation of polymer chains: freshly prepared solutions were used in each experiment and then discarded after the test, the total duration of each test (about 6 min) was kept well below the typical time scale for chain scission ($\simeq$ 12 min, see Ref. [3]), and the rotor speeds were traversed from low to high so as to minimize undue effects of degradation at the later steps.

Very recently, two semi-empirical models have been proposed in the literature to describe the mean velocity profile and frictional shear stress in the 'ultimate' regime of large Reynolds number Taylor-Couette turbulence. Cheng et al. [5] proposed a three-layer model comprising log-law velocity profiles near the two walls, matched to a central region of constant angular momentum equal to the average of the fluid angular momenta at the inner and outer cylinders. The wall shear stress at the (hydrodynamically smooth) inner cylinder then obeys the friction law

$$V^+ = \frac{4}{\kappa}\,\mathrm{W}\left[aZ(\zeta)\sqrt{\mathrm{Re}}\right], \tag{2}$$

where $\mathrm{W}(x)$ denotes the (principal branch of the) Lambert W function, the geometric factor

$$Z(\zeta) = \frac{\sqrt{\zeta}}{\sqrt{1-\zeta}} \tag{3}$$

is a function of the radius ratio ζ of the TC geometry, and the constant a is given by

$$a = \frac{\kappa}{8}\exp\left[\frac{\kappa}{8}(4A-1)\right] \simeq 0.117, \tag{4}$$

with the canonical values $\kappa = 0.4$ and $A = 4.5$ used for the von Kármán constant κ and the boundary layer offset parameter A, respectively. The skin friction predicted by Eq. 2 was validated against previous numerical and experimental results from the literature as well as by the authors' own

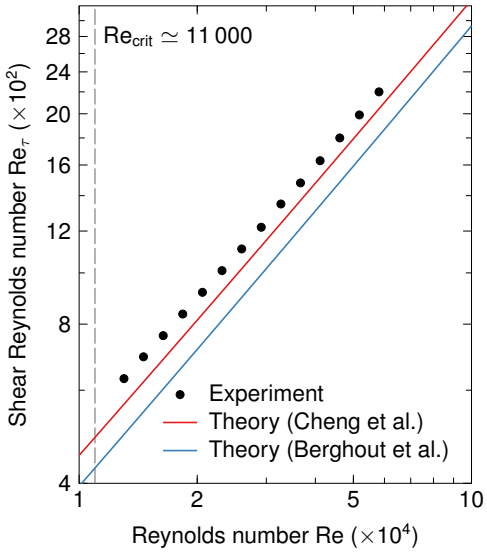

Figure S2. The experimental friction curve for the bespoke TC apparatus in featureless turbulent flow, compared to the semi-empirical models of Cheng et al. (Eq. 2) and Berghout et al. (Eq. 5), both evaluated for a radius ratio of $\zeta = 0.75$. For a given Newtonian fluid, notice that the abscissa Re is a function only of the rotor speed Ω (or equivalently, the wall speed V), whereas the ordinate Re_τ depends solely on the frictional torque $\mathcal{T}$ (or the wall shear stress τ_w). The above plot can thus be regarded as a non-dimensional representation of the "torque versus speed" characteristics of the TC apparatus in the turbulent regime.

wall-resolved large-eddy simulations (LES), for large Reynolds numbers $\mathrm{Re} \sim 10^5$–10^6 and radius ratios between 0.50 and 0.91 [5].

Berghout et al. [6] extended the three-layer model by introducing the curvature length scale $L_c = u_\tau/\kappa\,\Omega$, which separates regions near the wall where the production of turbulent kinetic energy is dominated by shear, and regions farther from the wall where it is influenced significantly by streamline curvature; the curvature length L_c is thus analogous to the Obukhov length in the Monin-Obukhov similarity theory for stratified shear flows. The resulting scale separation generates a new curvature boundary layer, overlying the usual Prandtl-von Kármán log-law layer, within which turbulent flow quantities scale with the curvature length L_c instead of the viscous length δ_ν. Asymptotic matching of the fluid angular velocity then yields a modified friction law for the inner wall [6], similar in form to Eq. 2:

$$V^+ = \frac{4}{\kappa}\,\mathrm{W}\left[bZ(\zeta)\sqrt{\mathrm{Re}}\right]\,. \tag{5}$$

The new empirical constant b is given by

$$b = \frac{\sqrt{\kappa}}{4}\exp\left[\frac{\kappa}{2}\left(C + \frac{\log\psi}{\lambda}\right)\right] \simeq 0.166\,, \tag{6}$$

where the model parameters $C = 1.0$, $\psi = 0.65$, and $\lambda = 0.64$ were inferred from fits to available experimental (PIV) and numerical (DNS) velocity profiles, at large rotation rates $10^8 \leqslant \mathrm{Ta} \leqslant 10^{12}$ and for radius ratios $0.50 \leqslant \zeta \leqslant 0.91$ [6].

Figure S2 compares the experimentally measured baseline for the TC apparatus [$\zeta = 0.75$, $Z(\zeta) = 1.732$] with the friction curves predicted by Eqs. 2 and 5; with the aspect ratio ζ fixed by design, there are no further adjustable parameters in either model. The baseline data shows good agreement with the three-layer model of Cheng et al. (Eq. 2); small deviations from the theoretical prediction ($\leqslant 12\,\%$, reduces to $\leqslant 8\,\%$ for $\mathrm{Re} \geqslant 37\,000$) can be attributed to end effects in rotor torque measurements, and perhaps more importantly, the relatively moderate range of operating Reynolds

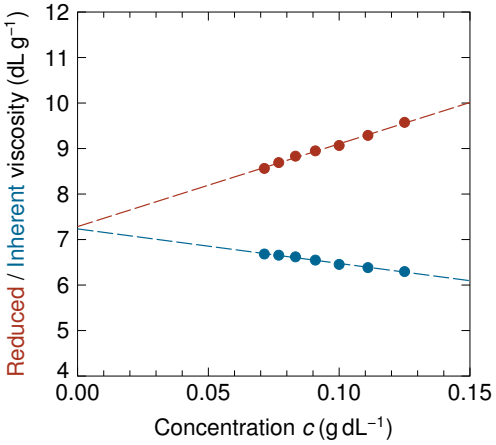

Figure S3. Huggins-Kraemer extrapolation of the reduced viscosity and the inherent viscosity to zero concentration, used to estimate the intrinsic viscosity of PAM chains dissolved in water.

numbers achieved in the TC apparatus (Re $\leqslant$ 60 000) and the attendant lack of strong scale separation or curvature effects as envisioned in the above models.

2. Characterization of polyacrylamide solutions

To measure the intrinsic viscosity $[\eta]$ of our PAM sample in water, we adopted the conventional method of successive dilution, in which we extrapolated both the reduced viscosity $\eta_{\mathrm{red}} = (\eta_0 - \eta_w)\,/\eta_w c$ and the inherent viscosity $\eta_{\mathrm{inh}} = \ln(\eta_0/\eta_w)\,/c$ concurrently to zero concentration [7]; here η_0 is the zero shear rate viscosity of the PAM solution, c the polymer concentration, and η_w the viscosity of the solvent (water). The zero shear rate viscosity η_0 at different concentrations was measured using a glass-capillary dilution viscometer of the Ubbelöhde type (Size 0B, Cannon Instrument Company), which was kept suspended in a water bath at controlled temperature. On extrapolation to zero concentration (see Fig. S3), both η_{red} and η_{inh} converge to a common intercept that represents the intrinsic viscosity $[\eta]$ of the dissolved polymer chains in solution [7]; this procedure yielded an intrinsic viscosity of $[\eta] = 7.26\,\mathrm{dL\,g^{-1}}$ for PAM in water. The intrinsic viscosity $[\eta]$ is related to the viscosity-averaged molar mass M_v via the empirical Mark-Houwink-Sakurada equation $[\eta] = KM_v^a$ [8]. Using values of the constants K and a for PAM available in the literature [9], we inferred a viscosity-averaged molar mass of approximately $M_v \simeq 2.54 \times 10^6\,\mathrm{g\,mol^{-1}}$ for our PAM sample. The critical overlap concentration c^* for flexible chains in good solvents may be estimated [8] as $c^* = 0.77/\,[\eta]$, yielding an overlap concentration of $c^* = 1.1\,\mathrm{g\,L^{-1}}$ for PAM chains dissolved in water. The solutions used in our flow tests are therefore in the dilute regime, with normalized concentrations in the range of $0.009 \leqslant c/c^* \leqslant 0.2$.

3. Polymer-mediated drag reduction in turbulent TC flow

When represented in Prandtl-von Kármán coordinates, drag reduction imparted by the dissolved polymer chains manifests as a higher slope and an upward divergence of the polymeric friction curves from the Newtonian baseline in the turbulent regime, as seen in Fig. 1(a) in the main text (reproduced herein as Fig. S4). Analogous to the behavior observed in turbulent pipe flows, the friction data for aqueous PAM solutions could be described by straight line fits on the Prandtl-von Kármán plot, of the form (see Eq. 2 in the main text)

$$V_P^+ = M_P \ln \mathrm{Re}_\tau + N_P, \tag{7}$$

which is similar in form to the pure solvent line, Eq. 1, albeit with a higher slope $M_P > M$ that varies with the polymer used as well as its concentration in the solution. The parameters M_P and N_P in Eq. 7, obtained by regression to the experimental data, are listed in Table S1 for aqueous PAM solutions

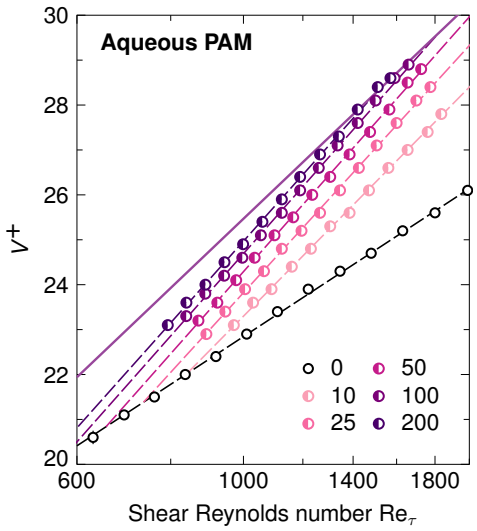

Figure S4. Experimental drag reduction curves, represented in Prandtl-von Kármán coordinates, for aqueous PAM solutions of different concentrations employed in this study. The legend indicates PAM concentration in ppm. The solid purple line denotes the maximum drag reduction estimate for solutions of flexible polymers in our bespoke TC geometry.

of different concentrations employed in this study. Following Virk [10], the point of drag reduction onset was estimated from the intersection of the polymeric friction curve, Eq. 7, with the Newtonian baseline; the corresponding shear Reynolds number at onset, Re_τ°, is also noted in Table S1 for various PAM concentrations c. In this context, it is pertinent to note once again that the flow state immediately preceding featureless turbulence in the TC fixture is one of turbulent Taylor vortices [11]—the pre-onset regime is not a simple laminar shear flow as in the case of pressure-driven pipe flows (or even TC flows with an outer rotating cylinder) wherein this preceding laminar state leads to a straightforward correspondence between the flow dynamics of the pure solvent and the dilute polymer solution [10].

In the canonical drag reduction phenomenology observed for viscoelastic flow through pipes, the friction curves become steeper and eventually merge onto a universal limiting curve, called the maximum drag reduction (MDR) asymptote, when either the polymer concentration or the shear Reynolds number is increased [10,12]. The MDR phenomenon in non-rotational shear flow geometries, such as pipe, channel, and boundary layer flows, has been extensively investigated and documented in numerous experimental and computational studies over the past several decades [10,13]. On the other hand, the gross flow behavior and drag reduction regimes of polymer solutions in turbulent rotational flows, such as Taylor-Couette turbulence, has hitherto remained poorly explored in the literature. Indeed, the only available information on the MDR asymptote in rotational flow configurations seems

Table S1. Properties of aqueous PAM solutions used in drag reduction experiments. The quantities listed for each solution, from left to right, are respectively the polymer concentration c, the normalized concentration c/c^*, the experimentally measured relative viscosity $\eta_r = \eta_0/\eta_w$, the friction curve fit parameters M_P and N_P in Eq. 7 (determined by linear regression from the Prandtl-von Kármán plot shown in Fig. S4), and the shear Reynolds number Re_τ° at the onset of drag reduction.

Concentration		**Relative viscosity**	**Friction curve**		**Drag reduction onset**
c (ppm)	c/c^*	η_r	M_P	N_P	Re_τ°
10	0.0094	1.01	7.36	−27.6	840
25	0.024	1.02	7.94	−31.0	736
50	0.047	1.04	8.19	−32.3	656
100	0.094	1.08	8.20	−32.0	585
200	0.19	1.15	8.13	−31.2	533

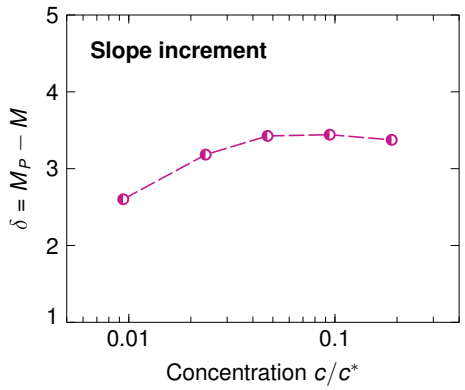

Figure S5. The slope increment δ for aqueous PAM solutions, as a function of the normalized polymer concentration c/c^*.

to be a relatively recent experimental study by Pereira et al. [14] using a double-gap concentric cylinder device. In this study, the MDR asymptote was estimated indirectly by deriving an empirical correlation for the percentage drag reduction and maximizing it with respect to the Reynolds number, polymer concentration, molecular weight, and the solution temperature [15]. Even so, MDR conditions were only approached, but not definitively realized, during actual experimental measurements. An in-depth study into the nature of the MDR state in rotational flows is thus required to address this critical gap in the literature; open questions yet to be conclusively settled include such fundamental issues as the dependence of the MDR asymptote on geometrical parameters, and whether such a limiting drag reduction curve (assuming one exists) is truly universal and independent of the polymer species, molecular weight, and chain flexibility. We note that in Taylor-Couette turbulence, unlike the case of pipe or channel flows, the Newtonian baseline is itself not universal in Prandtl-von Kármán variables, but is rather a function of the radius ratio of the annular gap employed [5,6]. The MDR curve too, by extension, cannot therefore be universal in the traditional sense, and would have to depend, at a minimum, on the radius ratio of the TC geometry; it is conceivable that it may also change with other experimental parameters, such as the macromolecular properties of the polymer additive.

In our case, a thorough investigation of the maximum drag reduction regime is constrained by operational limitations of our bespoke flow setup; specifically, at large polymer concentrations ($c/c^* \geqslant 0.25$), the increase in solution viscosity in the semi-dilute regime eventually leads to large frictional torques on the rotor that exceed the normal operating limits of the rheometer. Nevertheless, we can estimate a maximum drag reduction limit for flexible polymer additives in our bespoke TC apparatus, inferred from available experimental data corresponding to the largest elasticity numbers achieved in our flow setup for which we have reliable drag reduction measurements. For our particular TC geometry with a radius ratio of $\zeta = 0.75$, this estimated MDR line is given by

$$V^+ = 6.91 \ln \mathrm{Re}_\tau - 22.2 \,. \tag{8}$$

The above curve, denoted by the solid purple line in Fig. S4, was obtained using a semi-dilute solution of 2 MDa PEO dissolved in water ($c = 1460$ ppm, $c/c^* \simeq 1.72$, relaxation time $\lambda = 5.67$ ms, and elasticity number $\mathrm{El} = \lambda\eta/\rho d^2 \simeq 10^{-4}$); at these large polymer concentrations [i.e. $c/c^* \sim \mathcal{O}(1)$], individual friction curves on the Prandtl-von Kármán plot begin to approach each other, indicative of the attainment of MDR conditions (see Fig. 5b in Ref. [3]). From Fig. S4, we see that the PAM solutions employed in the present study mostly exhibit intermediate drag reduction in the LDR or HDR regimes, with only the 200 ppm solution ($c/c^* = 0.19$) reaching the MDR line at the highest Reynolds numbers. As a further corroboration, we also computed the *slope increment* $\delta = M_P - M$, as defined by Virk [16], for the polymeric friction curves in Fig. S4; the value of δ so obtained is shown as a function of the normalized concentration c/c^* in Fig. S5. The slope increment δ increases with concentration for

$c \leqslant 50$ ppm and then plateaus, again suggesting the approach to the MDR state at PAM concentrations beyond $c/c^* \simeq 0.1$.

As a final remark, we note that the maximum drag reduction limit indicated in Fig. S4 pertains only to solutions of *flexible* drag-reducing polymers in our TC fixture. Solutions of semi-flexible and rigid biopolymer chains, on the other hand, have been found to surpass this limit under suitable experimental conditions. This effect has been observed both in our own experiments using semiflexible mucilage polysaccharides [3], and was previously reported by Pereira et al. [14] in the case of xanthan gum, a rigid polysaccharide chain. Further investigation is required to fully elucidate the nature of this effect, and explain the maximum drag reduction behavior of flexible and rigid drag-reducing additives in rotating flows susceptible to centrifugal instabilities.

References

1. Srinivasan, S.; Kleingartner, J.A.; Gilbert, J.B.; Cohen, R.E.; Milne, A.J.B.; McKinley, G.H. Sustainable drag reduction in turbulent Taylor-Couette flows by depositing scalable superhydrophobic surfaces. *Phys. Rev. Lett.* **2015**, *114*, 014501.
2. Rajappan, A.; Golovin, K.; Tobelmann, B.; Pillutla, V.; Abhijeet.; Choi, W.; Tuteja, A.; McKinley, G.H. Influence of textural statistics on drag reduction by scalable, randomly rough superhydrophobic surfaces in turbulent flow. *Phys. Fluids* **2019**, *31*, 042107.
3. Rajappan, A.; McKinley, G.H. Epidermal biopolysaccharides from plant seeds enable biodegradable turbulent drag reduction. *Sci. Rep.* **2019**, *9*, 18263.
4. Lathrop, D.P.; Fineberg, J.; Swinney, H.L. Transition to shear-driven turbulence in Couette-Taylor flow. *Phys. Rev. A* **1992**, *46*, 6390–6405.
5. Cheng, W.; Pullin, D.I.; Samtaney, R. Large-eddy simulation and modelling of Taylor-Couette flow. *J. Fluid Mech.* **2020**, *890*, A17.
6. Berghout, P.; Verzicco, R.; Stevens, R.J.A.M.; Lohse, D.; Chung, D. Calculation of the mean velocity profile for strongly turbulent Taylor-Couette flow and arbitrary radius ratios. arXiv:2003.03294, 2020.
7. Pamies, R.; Cifre, J.G.H.; del Carmen López Martínez, M.; de la Torre, J.G. Determination of intrinsic viscosities of macromolecules and nanoparticles. Comparison of single-point and dilution procedures. *Colloid Polym. Sci.* **2008**, *286*, 1223–1231.
8. Rubinstein, M.; Colby, R.H. *Polymer Physics*; Oxford University Press, 2003.
9. McCarthy, K.J.; Burkhardt, C.W.; Parazak, D.P. Mark-Houwink-Sakurada constants and dilute solution behavior of heterodisperse poly(acrylamide-co-sodium acrylate) in 0.5 M and 1 M NaCl. *J. Appl. Polym. Sci.* **1987**, *33*, 1699–1714.
10. Virk, P.S. Drag reduction fundamentals. *AIChE J.* **1975**, *21*, 625–656.
11. Andereck, C.D.; Liu, S.S.; Swinney, H.L. Flow regimes in a circular Couette system with independently rotating cylinders. *J. Fluid Mech.* **1986**, *164*, 155–183.
12. Virk, P.S.; Mickley, H.S.; Smith, K.A. The ultimate asymptote and mean flow structure in Toms' phenomenon. *J. Appl. Mech.* **1970**, *37*, 488–493.
13. Xi, L. Turbulent drag reduction by polymer additives: fundamentals and recent advances. *Phys. Fluids* **2019**, *31*, 121302.
14. Pereira, A.S.; Andrade, R.M.; Soares, E.J. Drag reduction induced by flexible and rigid molecules in a turbulent flow into a rotating cylindrical double gap device: Comparison between poly (ethylene oxide), polyacrylamide, and xanthan gum. *J. Non-Newt. Fluid Mech.* **2013**, *202*, 72–87.
15. Pereira, A.S.; Soares, E.J. Polymer degradation of dilute solutions in turbulent drag reducing flows in a cylindrical double gap rheometer device. *J. Non-Newt. Fluid Mech.* **2012**, *179–180*, 9–22.
16. Virk, P.S.; Baher, H. The effect of polymer concentration on drag reduction. *Chem. Eng. Sci.* **1970**, *25*, 1183–1189.